

Date of publication xxxx xx, xxxx, date of current March 2, 2020.

Digital Object Identifier 10.1109/ACCESS.2020.DOI

W-net: Simultaneous segmentation of multi-anatomical retinal structures using a multi-task deep neural network

HONGWEI ZHAO¹, CHENGTAO PENG³, LEI LIU^{†2}, BIN LI^{†3}, Member, IEEE

¹School of Information Science and Technology, University of Science and Technology of China, Hefei, Anhui, 230022, China

²Department of Precision Machinery and Instrumentation, University of Science and Technology of China, Hefei, Anhui, 230022, China

³CAS Key Laboratory of Technology in Geo-spatial Information Processing and Application System, University of Science and Technology of China, Hefei, Anhui, 230026, China

†Corresponding author: Bin Li (e-mail: binli@ustc.edu.cn), Lei Liu (e-mail: liulei13@ustc.edu.cn)

This work is partially supported by the National Natural Science Foundation of China (Key Program) under grand No.U19B2044. It is supported by the GPU Computing Cluster of the data center, School of Information Science and Technology, University of Science and Technology of China.

ABSTRACT Segmentation of multiple anatomical structures is of great importance in medical image analysis. In this study, we proposed a \mathcal{W} -net to simultaneously segment both the optic disc (OD) and the exudates in retinal images based on the multi-task learning (MTL) scheme. We introduced a class-balanced loss and a multi-task weighted loss to alleviate the imbalanced problem and to improve the robustness and generalization property of the \mathcal{W} -net. We demonstrated the effectiveness of our approach by applying five-fold cross-validation experiments on two public datasets e_ophtha_EX and DiaRetDb1. We achieved F1-score of 94.76% and 95.73% for OD segmentation, and 92.80% and 94.14% for exudates segmentation. To further prove the generalization property of the proposed method, we applied the trained model on the DRIONS-DB dataset for OD segmentation and on the MESSIDOR dataset for exudate segmentation. Our results demonstrated that by choosing the optimal weights of each task, the MTL based \mathcal{W} -net outperformed separate models trained individually on each task. Code and pre-trained models will be available at: https://github.com/FundusResearch/MTL_for_OD_and_exudates.git.

INDEX TERMS Multi-task Learning, Unet, Optic Disc, Exudates

I. INTRODUCTION

It has been long that philosophers defined the eye as the window to the human soul. Indeed, more and more scientific and clinical evidences show that retina is indeed an extension of the central nervous system (CNS). During embryonic development, the retina and optic nerve extend from the diencephalon, and are thus considered part of the CNS [1]. The morphological variation in the retinal anatomical structures is of great diagnostic value, not only for the retinal pathology such as diabetic retinopathy (DR) [2], glaucoma [3], and age-related macular degeneration (AMD) [4], but also for the systemic heart- and brain-related diseases, such as hypertension, Parkinson's, and Alzheimer's diseases (AD) [5]. Since imaging of the retina with fundus photographs is non-invasive and inexpensive, many studies have been conducted to develop ocular biomarkers for AD or Parkinson's disease in the hope of potential wide implementation. Quantitative

analysis of the retinal anatomic structures, such as the optic disc (OD), optic cup (OC), blood vessels, and other pathological features like exudates and hemorrhage, is the first and essential step in the development of automated diagnostic or screening system.

OD segmentation is an essential step in detecting glaucoma, a chronic eye disease in which the optic nerve is gradually damaged. It is the second leading cause of blindness, with the global prevalence of 3.54% for population aged 40-80 years old [6]. If undiagnosed, glaucoma causes irreversible damage to the optic nerve leading to blindness. Therefore diagnosing glaucoma at early stages is extremely important for appropriate management and treatment of the disease [7]. The cup to disc ratio (CDR) is widely accepted and commonly used by clinicians to screen for glaucoma. The accurate segmentation of OD is critical to determine CDR. There are studies on the automatic segmentation of

arXiv:2006.06277v1 [eess.IV] 11 Jun 2020

OD in retinal images, which can be mainly grouped into four categories: morphological-based approaches [8], pixel classification methods [9], deformable model methods [10], and deep learning methods [11], [12]. In the group of morphological-based methods, Aquino *et al.* [8] presented a template-based methodology for segmenting the OD by using morphological and edge detection techniques followed by the circular Hough transformation. Another group of methods was proposed to transfer the boundary detection problem into a pixel classification task. Cheng *et al.* [9] used histograms and the center surround statistics to classify each pixel as disc or non-disc. Based on deformable model, Giachetti *et al.* [10] used ellipse fitting combined with a radial symmetry detector and a vessel density map to segment OD.

Deep convolutional neural network (DCNN) has been applied recently in retinal image processing. Huazhu Fu *et al.* [11] proposed a deep learning architecture (M-net), and Venkata Gopal Edupuganti *et al.* [12] applied a fully convolutional neural network (FCN) to solve OD segmentation problem.

Exudates are the early signs of diabetic retinopathy (DR), which caused 2.6% of blindness worldwide in 2010 [13]. Exudates are lipid and lipoprotein deposits that appear near leaking capillaries within the retina. They develop at the early stage of DR and may appear as yellow areas with variable sizes from a few pixels to as large as the optic disc (Fig. 1(a)). After 20 years of diabetes, nearly all patients with Type I diabetes and >60% of patients with Type II diabetes have some degree of retinopathy [14]. Though the exudates and OD may look very different, they do share some similarity, for example, both of them appear as bright yellow areas in color fundus photographs. Thresholding methods, based on either global or local image gray-levels [15], [16], or clustering-based image thresholding, such as Otsu thresholding [16], had been applied for exudate segmentation. J. Kaur *et al.* [17] proposed a dynamic decision thresholding method to reliably segment exudates irrespective of the associated heterogeneity, brightness and faint edges of the image. Region growing methods [18] were demonstrated for automatic segmentation of exudates, particularly in combination with the artificial neural network [19]. In the category of machine learning based methods, Benalcázar *et al.* [20] used logistic regression to classify each exudate candidate detected by the ensemble of aperture filters. Giancardo *et al.* [21] segmented exudates using features extracted manually in combination with support vector machine (SVM).

DCNNs have been proven to outperform conventional image analysis methods in many aspects, especially because they do not require explicit feature extraction. Recently, deep learning methods were applied to detect exudates and OD in color fundus photographs and showed promising results [22], [23]. However, these methods delineated one kind of anatomy at a time.

In contrast, multi-task learning [24] seeks to simultane-

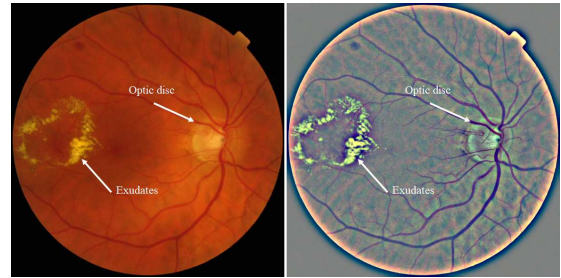


FIGURE 1: (a) A retina image with labeled exudates and the optic disc. (b) The preprocessed image of (a) using Eq.(1).

ously learn a set of task-specific classification or regression models. The rationale behind MTL is that by utilizing the correlation information among the related tasks, a joint learning method is much more efficient than learning each task separately. MTL has been successfully employed in image classification [25], visual tracking [26], multi-view action recognition [27] and egocentric daily activity recognition [28]. However, to the best of our knowledge, there was no study of using MTL in the retinal anatomy segmentation.

In the study, based on the multi-task deep learning scheme, we constructed a \mathcal{W} -net to simultaneously segment both OD and exudates. By utilizing the correlation between the tasks, the network showed better performance than individual one-task only networks. This method was ready to apply to other multi-task scenarios, especially in the field of medical image analysis.

II. MATERIALS AND METHODS

Based on the MTL scheme, we proposed a \mathcal{W} -net to simultaneously segment OD and exudates. We trained our model using two datasets: e_ophtha_EX [29] and DiaRetDb1 [30], but tested on four datasets: e_ophtha_EX [29], DiaRetDb1 [30], DRIONS-DB [31] and MESSIDOR [32].

A. DATASETS

The e_ophtha_EX dataset consists of 82 fundus images. There are four different image sizes of 1440×960 or 1504×1000 or 2544×1696 or 2048×1360 pixels. All the images were acquired with a 45-degree field of view. The dataset contains 47 images with exudates and 35 images with no lesion. This dataset does not provide the ground truth for the optic discs. With the help of an ophthalmologist, we manually annotated the OD pixels for all the 82 images.

The DiaRetDb1 [30] dataset contains 89 color fundus images, which were captured using the same 50 degree field-of-view digital fundus camera with varying imaging settings. There are 26 images containing exudates with annotated ground truth [33]. We manually annotated the OD pixels of all the 89 images.

The DRIONS-DB dataset [31] consists of 110 images of 600×400 pixels. All the ground truths of the OD pixels are provided. This public dataset was widely used to evaluate the performance of OD segmentation algorithms.

The MESSIDOR [32] dataset consist of 1200 TIFF images with three different image sizes, 1440×960, 2240×1488 and 2304×1536 pixels. All the images were acquired with a color video CDD camera on a TopCon TRC NW6 with a 45-degree field of view. There are 226 images consisting of exudates and 974 images without exudates. We used 226 images with exudates and groundtruth images from [34].

B. IMAGE PREPROCESSING

All the images were rescaled to 576×576 pixels. If the original images were smaller (for example images in the DRIONS-DB dataset), we applied zero-padding. The pre-processed image I_p was evaluated using Eq.(1) [35]

$$I_p = \alpha \cdot I + \beta \cdot I_{Gauss} + \gamma \tag{1}$$

where α , β , and γ were set to 4, -4, and 128, respectively. I_{Gauss} , the Gaussian blurred image was obtained with a 9×9 Gaussian kernel.

C. S-NET AND W-NET STRUCTURES

We constructed a single task network (S -net), which was based on a U-net [36] (Fig. 2(a)). As shown in Fig. 2(b), the S -net had an encoder and a decoder. The encoder path was responsible for the feature extraction, same as the U-net, while the decoder path was different with U-net in that every output of the upsampling layer was concatenated with the output of the last upsampling layer.

The proposed multi-task W -net was based on the S -net by adding a second decoder path for the second task, as shown in Fig. 3. The two decoders shared the same encoder and generated the OD and exudates segmentations, respectively. The details of the configuration of the network were listed in Table 1. In the encoder path, two convolutional layers, both with a 3×3 kernel, were followed by normalization and dropout with a rate of 0.2. A leaky rectified linear unit (LeakyReLU) was implemented as the activation function. A 2×2 max pooling with a stride of two at each dimension was applied. In the decoder path, similar to the encoder path, two 3×3 convolutional layers were followed by a LeakyReLU activation. An upsampling layer with a kernel size of 2×2 and a stride of two in each dimension was applied and the output was fused with the corresponding layers in the encoder path. In the last layer, a 1×1 convolution reduced the number of output channels to 2. The input of the network was 576×576 and the output image size was the same as the input. In the decoder path of S -net, the output of each upsampling layer was concatenated with the output of the last upsampling layer.

D. LOSS FUNCTIONS

We defined the multi-task total loss $\mathcal{L}_{total}(x, \theta)$, the OD task loss $\mathcal{L}_{OD}(x; \theta)$, and the exudate task loss $\mathcal{L}_{EX}(x; \theta)$.

For easy reading, we applied the same symbols as used in the study by Maninis *et al.* [37]. Briefly, the training

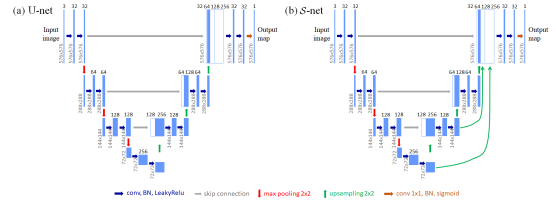


FIGURE 2: (a) An U-net structure. (b) The proposed single-task network structure (S -net). The network was improved based on an U-net. In the decoder path of S -net, the output of each upsampling layer was concatenated with the output of the last upsampling layer.

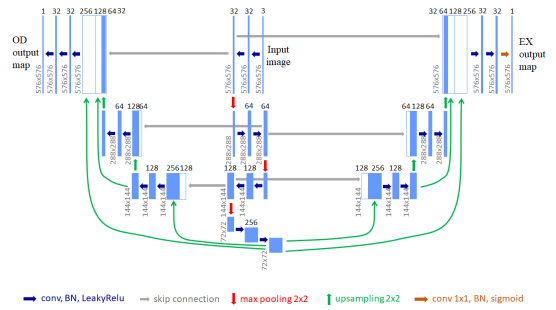


FIGURE 3: The structure of the proposed W -net. The encoder (middle) was shared by the two decoders, which were used to segment the OD and exudates, respectively. Like in the U-net, the corresponding encoder layers and the decoder layers were skip connected. In addition, the same as the S -net, the output of each upsampling layer was concatenated to the last upsampling layer in the decoder.

dataset was denoted as $S = (X_m, Y_m, Z_m), m = 1, \dots, M$, where M was the total number of images with X_m being the input image. $Y_m = \{y_i^{(m)} | i = 1, \dots, N, |X_m, y_i^{(m)} \in \{0, 1\}\}$ and $Z_m = \{z_i^{(m)} | i = 1, \dots, N, |X_m, z_i^{(m)} \in \{0, 1\}\}$ were the predicted pixel-wise labels of optic disc and exudates, respectively. The loss functions were then defined as:

$$\mathcal{L}_{total}(x, \theta) = \omega \cdot \mathcal{L}_{EX}(x; \theta) + (1 - \omega) \cdot \mathcal{L}_{OD}(x; \theta) \tag{2}$$

$$\mathcal{L}_{EX} = -\frac{1}{m} \sum_{m=1}^M [-\lambda_2 \sum_{i \in Z_+} \log P(z_i^{(m)} = 1 | X^{(m)}; \theta) - (1 - \lambda_2) \sum_{i \in Z_-} \log P(z_i^{(m)} = 0 | X^{(m)}; \theta)] \tag{3}$$

$$\mathcal{L}_{OD} = -\frac{1}{m} \sum_{m=1}^M [-\lambda_1 \sum_{i \in Y_+} \log P(y_i^{(m)} = 1 | X^{(m)}; \theta) - (1 - \lambda_1) \sum_{i \in Y_-} \log P(y_i^{(m)} = 0 | X^{(m)}; \theta)] \tag{4}$$

TABLE 1: The detailed configurations of the \mathcal{W} -net

Encoder path	Output size	Decoder path1	Output size	Decoder path2	Output size
Conv1 32 3×3	576×576				
Conv2 32 3×3	576×576	A_Conv7 2 1×1	576×576	B_Conv7 2 1×1	576×576
Max pooling 2×2	288×288	A_Conv6 32 3×3	576×576	B_Conv6 32 3×3	576×576
Conv3 64 3×3	288×288	A_Conv5 32 3×3	576×576	B_Conv5 32 3×3	576×576
Conv4 64 3×3	288×288	Upsampling 2×2	576×576	Upsampling 2×2	576×576
Max pooling 2×2	144×144	A_Conv4 64 3×3	288×288	B_Conv4 64 3×3	288×288
Conv5 128 3×3	144×144	A_Conv3 64 3×3	288×288	B_Conv3 64 3×3	288×288
Conv6 128 3×3	144×144	Upsampling 2×2	288×288	Upsampling 2×2	288×288
Max pooling 2×2	72×72	A_Conv2 128 3×3	144×144	B_Conv2 128 3×3	144×144
Conv7 256 3×3	72×72	A_Conv1 128 3×3	144×144	B_Conv1 128 3×3	144×144
Conv8 256 3×3	72×72	Upsampling 2×2	144×144	Upsampling 2×2	144×144

where θ denoted the parameters of our \mathcal{W} -net. Y_+ and Y_- represented the positive and negative label sets of the optic disc, respectively. Z_+ and Z_- represented the exudates and non-exudates ground truth label sets, respectively. The probability $P(y_i^{(m)} = 1|X^{(m)}; \theta) \in [0, 1]$ was computed using sigmoid function on the activation value at each pixel. We used $\lambda_1 = 0.7$ and $\lambda_2 = 0.9$ to alleviate the imbalance of the substantially greater number of background compared to the foreground pixels. It is important to choose the correct λ_1 and λ_2 in Eq.(3, 4). ω was the loss equilibrium parameter, which balanced the two different tasks. We applied the method proposed by Xie *et al.* [38], which used the ratio of the number of the background pixels and the number of pixels of the whole image.

E. TRAINING AND TESTING OF THE NETWORKS

We adapted five-fold cross-validation to evaluate the generalization property of the networks. Each dataset was splitted into 5 subsets of nearly equal size. Five independent models of each of the U-net, \mathcal{S} -net, and \mathcal{W} -net were trained. The models were trained on 4 splits (80%) and tested on the remaining split (20%) to assess the ability to generalize to the previously unseen images.

During training, we did data augmentation by rotating the image with a random angle, flipping image randomly or adding random Uniform noise($U(0.8, 1.2)$) to the image. In addition, the images were normalized by subtracting the averages of the pixels from each image and divided by the standard deviation. We initialized the weights in each layer from a zero-mean Gaussian distribution with a standard deviation of $0.01(\mathcal{N}(0, 0.01))$. We trained the networks for 1000 epochs with a batch size of 2, and with an Adam optimizer with a learning rate of 0.0005 and β of 0.5.

III. RESULTS

A. EVALUATION METRICS

We evaluated the performance of the network both on the exudate and the OD segmentation. We applied the lesion

level measurement for the exudates [29], [39], and the overlapping score metric for the OD segmentation [8]. For the lesion level evaluation, we compared the predicted candidates with the ground truth provided in the datasets. We applied the approach based on set operations [29], [39]. Briefly, if the two sets had enough overlap as controlled by an overlapping factor σ , which was set to 0.2 in our study, the same as the work [29], the candidates were considered correctly classified. We computed the sensitivity, precision, and the F1-score according to the equations defined in Table 2.

TABLE 2: Definitions of the evaluation metrics

Performance Measure	Mathematical Formula
Accuracy	$(TP+TN)/(TP+TN+FN+FP)$
Sensitivity	$TP/(FN+TP)$
Specificity	$TN/(FP+TN)$
Precision	$TP/(FP+TP)$
F1-Score	$2*TP/(2*TP+FP+FN)$

¹ TP stands for true positive. FP: false positive; TN: true negative; FN: false negative.

In order to compare our OD segmentation results with previous studies, we applied the overlapping score. Overlapping score (η) was a common evaluation metric for OD segmentation assessment [8]. η was defined as:

$$\eta = \frac{Area(P \cap G)}{Area(P \cup G)} \quad (5)$$

where P and G denoted the predicted and manually annotated OD regions, respectively.

B. COMPARISONS OF THE \mathcal{S} -NET AND THE U-NET

To compare the performance of the \mathcal{S} -net and the U-net, we conducted the OD segmentation and the exudate segmentation on the e_ophtha_EX and DiaRetDb1 datasets. As shown in Table 3, for the OD segmentation, on the

TABLE 3: Results of the OD segmentation using the U-net and the \mathcal{S} -net on the two datasets

Experiments		F1-score	Sensitivity	Precision	η
e_ophtha_EX	U-net	93.84% $\pm 1.71\%$	92.81% $\pm 1.86\%$	94.91% $\pm 1.64\%$	88.45% $\pm 2.97\%$
	\mathcal{S} -net	93.46% $\pm 2.79\%$	92.31% $\pm 4.20\%$	94.69% $\pm 1.31\%$	87.84% $\pm 4.75\%$
DiaRetDb1	U-net	95.33% $\pm 0.78\%$	94.65% $\pm 1.21\%$	96.03% $\pm 0.79\%$	91.08% $\pm 1.44\%$
	\mathcal{S} -net	95.42% $\pm 0.81\%$	94.76% $\pm 1.66\%$	96.10% $\pm 0.54\%$	91.25% $\pm 1.48\%$

TABLE 4: Results of the exudate segmentation using the U-net and the \mathcal{S} -net on the two datasets

Experiments		F1-score	Sensitivity	Precision
e_ophtha_EX	U-net	91.14% \pm 0.94%	92.87% \pm 2.81%	89.57% \pm 1.65%
	\mathcal{S} -net	91.57% \pm 1.01%	92.74% \pm 1.26%	90.47% \pm 1.95%
DiaRetDb1	U-net	90.68% \pm 2.63%	89.21% \pm 3.52%	92.28% \pm 2.76%
	\mathcal{S} -net	91.25% \pm 2.59%	89.57% \pm 3.31%	93.06% \pm 2.86%

TABLE 5: Results of the OD segmentation using the \mathcal{S} -net and \mathcal{W} -net on the two datasets

Experiments		F1-score	Sensitivity	Precision	η
e_ophtha_EX	\mathcal{S} -net	93.46% $\pm 2.79\%$	92.31% $\pm 4.20\%$	94.69% $\pm 1.31\%$	87.84% $\pm 4.75\%$
	\mathcal{W} -net	94.76% $\pm 1.23\%$	93.81% $\pm 2.33\%$	95.77% $\pm 0.46\%$	90.07% $\pm 2.21\%$
DiaRetDb1	\mathcal{S} -net	95.42% $\pm 0.81\%$	94.76% $\pm 1.66\%$	96.10% $\pm 0.54\%$	91.25% $\pm 1.48\%$
	\mathcal{W} -net	95.73% $\pm 0.66\%$	95.07% $\pm 0.82\%$	96.39% $\pm 0.52\%$	91.81% $\pm 1.22\%$

TABLE 6: Results of the exudate segmentation using the \mathcal{S} -net and \mathcal{W} -net on the two datasets

Experiments		F1-score	Sensitivity	Precision
e_ophtha_EX	\mathcal{S} -net	91.57% \pm 1.01%	92.74% \pm 1.26%	90.47% \pm 1.95%
	\mathcal{W} -net	92.80% \pm 0.79%	92.65% \pm 1.15%	92.97% \pm 1.67%
DiaRetDb1	\mathcal{S} -net	91.25% \pm 2.59%	89.57% \pm 3.31%	93.06% \pm 2.86%
	\mathcal{W} -net	94.14% \pm 1.62%	93.26% \pm 3.27%	95.12% \pm 1.12%

e_ophtha_EX dataset, the U-net was slightly better than the \mathcal{S} -net, while on the DiaRetDb1 dataset, the \mathcal{S} -net was slightly better. However, for the exudate segmentation, as listed in Table 4, the F1-score achieved by the \mathcal{S} -net was higher than that by the U-net ($p = 0.08$). Therefore, we chose the \mathcal{S} -net as the building block for the \mathcal{W} -net.

C. THE \mathcal{W} -NET IMPROVED BOTH THE OD AND EXUDATE SEGMENTATION PERFORMANCE

The \mathcal{W} -net outperformed the \mathcal{S} -net for both OD and exudate segmentation. As shown in Fig. 4, on both datasets, the \mathcal{W} -net demonstrated better performance for both OD and exudate segmentation than the \mathcal{S} -net, as evaluated using F-1 score, sensitivity, and precision. Particularly, for the exudate segmentation the F-1 score achieved using the \mathcal{W} -net was more than 2% higher than that achieved using the \mathcal{S} -net ($p < 0.05$) on the two datasets. The F-1 score is a

more comprehensive performance metric than the sensitivity or the precision. For the OD segmentation, the \mathcal{W} -net also showed better performance than the \mathcal{S} -net though the difference was not as significant as the improvement in the exudate segmentation. Table 5 and Table 6 listed all the values.

Fig. 5 showed the precision-recall (PR) curves with the area under curves (AUCs) of the \mathcal{S} -net and \mathcal{W} -net. Each curve was the average of the five cross-validation results. For OD segmentation, the AUCs using the \mathcal{S} -net were 0.9727, 0.9900 on the e_ophtha_EX and the DiaRetDb1 datasets respectively, compared with 0.9833 and 0.9921 using the \mathcal{W} -net. For the exudate segmentation, with the \mathcal{W} -net the AUCs were 0.9720 and 0.9734 compared with 0.9652 and 0.9581 using the \mathcal{S} -net as tested on the e_ophtha_EX and the DiaRetDb1 datasets, respectively. The average curve of the \mathcal{W} -net completely enclosed the curve of the \mathcal{S} -net,

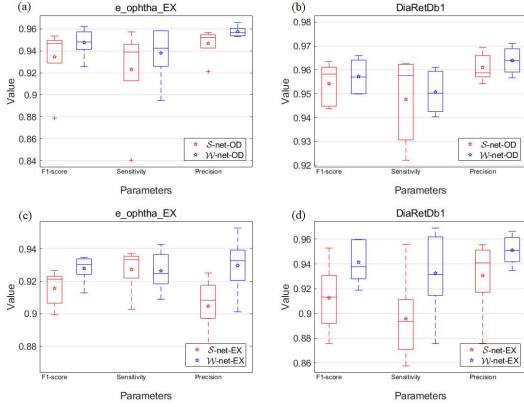


FIGURE 4: The comparisons of the performance of the S -net and the W -net using five-fold cross-validation. The first row (a and b) showed the comparison of the OD segmentation as tested on the e_ophtha_EX and the DiaRetDb1 datasets. The second row (c and d) compared the performance of the exudate segmentation using the same two datasets.

demonstrating the better performance of the proposed W -net. Fig. 6 showed the segmentation results of the S -net and W -net on the e_ophtha_EX and the DiaRetDb1 datasets.

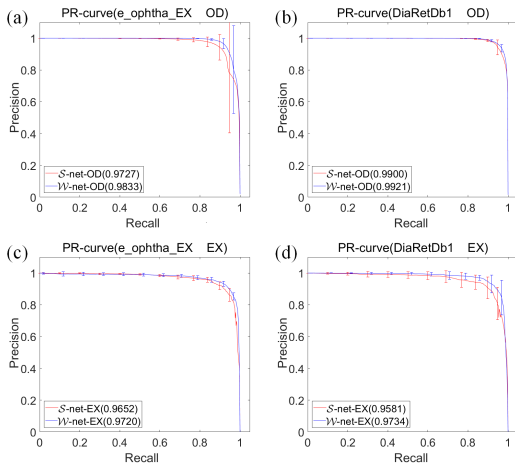


FIGURE 5: The comparisons of PR curves of the S -net and W -net using five-fold cross-validation. The first row (a and b) showed the comparison of the OD segmentation as tested on the e_ophtha_EX and the DiaRetDb1 datasets. The second row (c and d) compared the performance of the exudate segmentation using the same two datasets. Comparing with S -net, it's obvious that the W -net has achieved higher AUCs of the PR curves in both exudates and optic disc segmentation task in two datasets.

From the images, we can see that the false positive and false negative of the S -net is more than the W -net. The green areas, namely true positive, of the W -net takes up a greater proportion than that of the S -net. From the

TABLE 7: Results of the OD segmentation on DRIONS-DB dataset and exudate segmentation on the MESSIDOR dataset using the S -net and W -net

Experiments		F1-score	Sensitivity	Precision
DRIONS-DB(OD)	S -net	89.91%	89.27%	90.36%
	W -net	95.57%	95.50%	95.64%
MESSIDOR(EX)	S -net	91.36%	92.94%	89.83%
	W -net	92.66%	95.32%	90.15%

figure, it is intuitive to see that the W -net achieved better performance than the S -net.

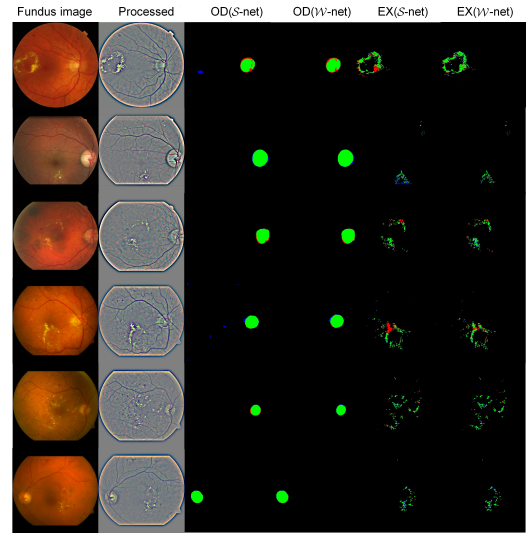


FIGURE 6: The first three rows displayed images of the e_ophtha_EX dataset and the last three rows showed images of the DiaRetDb1 dataset. The first column listed the RGB images. The second column listed the preprocessed images, and the third and fourth columns listed the segmented ODs using the S -net and W -net, respectively. The last two columns illustrated the segmented exudates using the S -net and W -net, respectively. The green areas represented the correctly predicted lesions by algorithms (true positive), the red areas represented lesions not predicted by algorithms (false negative), and the blue areas represented the falsely predicted lesions by the algorithms (false positive).

D. THE W -NET IMPROVED THE THE ROBUSTNESS AND GENERALIZATION OF THE NETWORK

To compare the robustness and generalization properties of the S -net and W -net, we applied the trained S -net and W -net to test OD and exudates segmentation on the DRIONS-DB and MESSIDOR datasets, respectively. Both the DRIONS-DB and MESSIDOR datasets were not applied to train the models. Table 7 showed the performance of the S -net and W -net on the two datasets. From the table, it is clear that the W -net is superior to the S -net for the performance of the OD and exudates segmentation.

TABLE 8: Comparison of the performances of the OD segmentation of our method with previous published methods on two public datasets

Dataset	Methodology	η	F1-score	Sensitivity	Precision
DiaRetDb1	Walter <i>et al.</i> [42]	36.97%	-	65.69%	-
	Abdullah <i>et al.</i> [43]	85.1%	89.10%	85.08%	-
	Morales <i>et al.</i> [44]	-	89.30%	-	-
	Proposed	91.81%	95.73%	95.07%	96.39%
DRIONS-DB	Walter <i>et al.</i> [42]	-	68.13%	-	-
	Zahoor <i>et al.</i> [45]	88.6%	-	93.84%	-
	Abdullah <i>et al.</i> [43]	85.1%	91.02%	85.1%	-
	Proposed	91.52%	95.57%	95.50%	95.64%

TABLE 9: Comparison of the performance of the exudate segmentation of the \mathcal{W} -net with previous published methods on the two public datasets

Database	Methodology	Accuracy	Specificity	Sensitivity	Precision
e_ophtha_EX	Moazam <i>et al.</i> [46]	89.25%	94.60%	81.20%	90.91%
	Zhang <i>et al.</i> [29]	--	--	74%	79%
	Proposed	99.97%	99.99%	92.65%	92.97%
DiaRetDb1	B Harangi <i>et al.</i> [47]	-	-	85%	84%
	Moazam <i>et al.</i> [46]	87.72%	81.25%	92.42%	87.14%
	Zheng <i>et al.</i> [34]	99.97%	99.98%	93.94%	91.02%
	Proposed	99.98%	99.99%	93.26%	95.12%

The \mathcal{W} -net surpassed the \mathcal{S} -net more than 5.6% of F1-score on OD segmentation on the DRIONS-DB dataset and exceeded more than 1.3% on exudates segmentation on the MESSIDOR dataset. It is conclusive that the robustness and generalization of the \mathcal{W} -net are much better than the \mathcal{S} -net.

IV. DISCUSSION

Simultaneous segmentation of multiple anatomical structures is of great importance in medical image analysis. Most existing DCNNs apply independent networks for each individual task and completely ignore the correlation information among tasks. To utilize the correlation among different tasks, we proposed a \mathcal{W} -net to simultaneously segment both OD and exudates. These two tasks shared the same encoder path, which greatly reduced the risk of overfitting [40]. Indeed, the work by Baxter *et al.* [41] showed that the risk of overfitting the shared parameters was order N smaller than that of fitting the task-specific parameters, where N was the number of tasks.

Another advantage of the MTL based \mathcal{W} -net was the significant reduction of the fitting parameters. The \mathcal{W} -net had 2.9M trainable parameters, while the two \mathcal{S} -nets had 4.1M parameters. The \mathcal{W} -net was not only more efficient in the training stage, but also faster in the testing stage than the \mathcal{S} -net. For instance, to finish an image using the \mathcal{W} -net need 0.15 seconds while it took 0.22 seconds using two \mathcal{S} -net sequentially on an Intel Core i7-7700 CPU with Nvidia GeForce GTX 1080 Ti. This is important where long computation time is prohibitive.

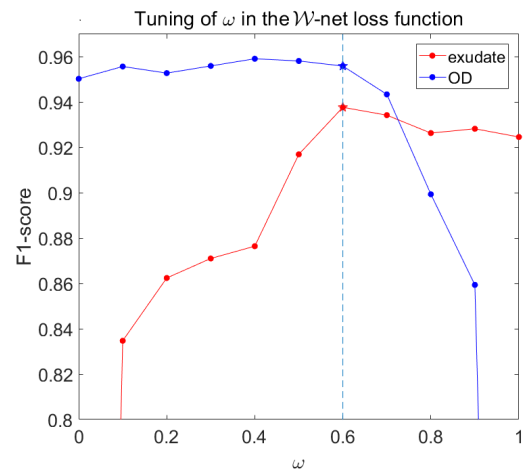


FIGURE 7: The F1-score of exudate and OD segmentation vs different loss weight on the DiaRetDb1 dataset.

We compared our results with recently published literature on OD (Table 8) and exudate segmentation (Table 9). Since most of the published work on OD segmentation used DRIONS-DB dataset to evaluate the performance of the segmentation algorithms, we applied the \mathcal{W} -net on the same dataset for comparison. As shown in Table 8, our proposed \mathcal{W} -net outperformed other methods on both datasets by a large margin as evaluated by either η , F1-score, sensitivity or precision.

Table 9 showed the comparison on the exudate segmenta-

tion. We made sure that all the studies listed used the same lesion level evaluation method [39] as used in our study to keep a fair comparison. From the table, it was clear that our proposed \mathcal{W} -net surpassed most of the methods published except the method proposed by Zheng *et al.* [34] in sensitivity. However, we noticed that Zheng *et al.* applied an ensemble method instead of using a single network.

As illustrated in the reference [48], the performance of a multi-task deep convolutional neural network is strongly dependent on the relative weight between the loss of each task. This is manifested in the tuning of the ω parameter in Eq. 2. Kendall *et al.* [48] proposed a method to choose the optimal weights by considering the homoscedastic uncertainty of each task. In this study, we applied a more conventional method by scanning the value of ω from 0 to 1 with an incremental step size of 0.1. As shown in Fig. 7, the \mathcal{W} -net achieved best performance of both OD and exudate segmentation on DiaRetDb1 dataset when ω was set to 0.6.

V. CONCLUSION

In summary, we sought to develop a deep neural network combined with MTL for simultaneous exudate and OD segmentation. Based on the \mathcal{S} -net, an improved version of U-net, we developed a \mathcal{W} -net, which demonstrated excellent performance when compared with previous studies. Compared with applying two \mathcal{S} -net sequentially, \mathcal{W} -net was more efficient and robust. The recent study by Kendall *et al.* [48]–[50] came to the same conclusion that by optimally weighting loss terms in the multi-task loss function, the multi-task model outperformed separate models trained individually on each task. This method can be readily applied to more than two tasks. One of the difficulties of applying such method was due to the lack of multi-labeled datasets, which is a general problem in the application of deep neural networks. Though in this study, both tasks were applied on the fundus images, MTL method could be used to process images from different modalities, for example, images from optical coherence tomography (OCT) in combination with ultrasound.

VI. ACKNOWLEDGMENT

The work is partially supported by the National Natural Science Foundation of China (Key Program) under grand No.U19B2044. It is supported by the GPU Computing Cluster of the data center, School of Information Science and Technology, University of Science and Technology of China.

REFERENCES

- [1] A. London, I. Benhar, and M. Schwartz, "The retina as a window to the brain—from eye research to CNS disorders," *Nature Reviews Neurology*, vol. 9, no. 1, pp. 44–53, Jan. 2013.
- [2] A. Sopharak, B. Uyyanonvara, S. Barman, and T. H. Williamson, "Automatic detection of diabetic retinopathy exudates from non-dilated retinal images using mathematical morphology methods," *Computerized medical imaging and graphics*, vol. 32, no. 8, pp. 720–727, 2008.
- [3] G. D. Joshi, J. Sivaswamy, and S. Krishnadas, "Optic disk and cup segmentation from monocular color retinal images for glaucoma assessment," *IEEE transactions on medical imaging*, vol. 30, no. 6, pp. 1192–1205, 2011.
- [4] L. S. Lim, P. Mitchell, J. M. Seddon, F. G. Holz, and T. Y. Wong, "Age-related macular degeneration," *The Lancet*, vol. 379, no. 9827, pp. 1728–1738, 2012.
- [5] S. McGrory, J. R. Cameron, E. Pellegrini, C. Warren, F. N. Doubal, I. J. Deary, B. Dhillon, J. M. Wardlaw, E. Trucco, and T. J. MacGillivray, "The application of retinal fundus camera imaging in dementia: A systematic review," *Alzheimer's & Dementia: Diagnosis, Assessment & Disease Monitoring*, vol. 6, pp. 91–107, 2017.
- [6] Y.-C. Tham, X. Li, T. Y. Wong, H. A. Quigley, T. Aung, and C.-Y. Cheng, "Global prevalence of glaucoma and projections of glaucoma burden through 2040: a systematic review and meta-analysis," *Ophthalmology*, vol. 121, no. 11, pp. 2081–2090, 2014.
- [7] R. Hitchings, "European glaucoma society terminology and guidelines for glaucoma, -part 1 supported by the egs foundation foreword," 2017.
- [8] A. Aquino, M. E. Gegúndez-Arias, and D. Marín, "Detecting the optic disc boundary in digital fundus images using morphological, edge detection, and feature extraction techniques," *IEEE transactions on medical imaging*, vol. 29, no. 11, pp. 1860–1869, 2010.
- [9] J. Cheng, J. Liu, Y. Xu, F. Yin, D. W. K. Wong, N.-M. Tan, D. Tao, C.-Y. Cheng, T. Aung, and T. Y. Wong, "Superpixel classification based optic disc and optic cup segmentation for glaucoma screening," *IEEE Transactions on Medical Imaging*, vol. 32, no. 6, pp. 1019–1032, 2013.
- [10] A. Giachetti, L. Ballerini, and E. Trucco, "Accurate and reliable segmentation of the optic disc in digital fundus images," *Journal of Medical Imaging*, vol. 1, no. 2, p. 024001, 2014.
- [11] H. Fu, J. Cheng, Y. Xu, D. W. K. Wong, J. Liu, and X. Cao, "Joint optic disc and cup segmentation based on multi-label deep network and polar transformation," *IEEE Transactions on Medical Imaging*, 2018.
- [12] V. G. Edepuganti, A. Chawla, and A. Kale, "Automatic optic disk and cup segmentation of fundus images using deep learning," in *2018 25th IEEE International Conference on Image Processing (ICIP)*. IEEE, 2018, pp. 2227–2231.
- [13] R. R. Bourne, G. A. Stevens, R. A. White, J. L. Smith, S. R. Flaxman, H. Price, J. B. Jonas, J. Keeffe, J. Leasher, K. Naidoo et al., "Causes of vision loss worldwide, 1990–2010: a systematic analysis," *The Lancet Global Health*, vol. 1, no. 6, pp. e339–e349, 2013.
- [14] A. D. Association, *Diabetes*. American Diabetes Association, 1966, no. 7-12.
- [15] R. Phillips, J. Forrester, and P. Sharp, "Automated detection and quantification of retinal exudates," *Graefes' archive for clinical and experimental ophthalmology*, vol. 231, no. 2, pp. 90–94, 1993.
- [16] K. Wisaeng, N. Hiransakolwong, and E. Pothiruk, "Automatic detection of exudates in retinal images based on threshold moving average models," *Biophysics*, vol. 60, no. 2, pp. 288–297, 2015.
- [17] J. Kaur and D. Mittal, "A generalized method for the segmentation of exudates from pathological retinal fundus images," *Biocybernetics and Biomedical Engineering*, vol. 38, no. 1, pp. 27–53, 2018.
- [18] B. M. Ege, O. K. Hejlesen, O. V. Larsen, K. Møller, B. Jennings, D. Kerr, and D. A. Cavan, "Screening for diabetic retinopathy using computer based image analysis and statistical classification," *Computer methods and programs in biomedicine*, vol. 62, no. 3, pp. 165–175, 2000.
- [19] D. Usher, M. Dumskyj, M. Himaga, T. H. Williamson, S. Nussey, and J. Boyce, "Automated detection of diabetic retinopathy in digital retinal images: a tool for diabetic retinopathy screening," *Diabetic Medicine*, vol. 21, no. 1, pp. 84–90, 2004.
- [20] M. Benalcázar, M. Brun, and V. Ballarin, "Automatic segmentation of exudates in ocular images using ensembles of aperture filters and logistic regression," in *Journal of Physics: Conference Series*, vol. 477, no. 1. IOP Publishing, 2013, p. 012021.
- [21] L. Giancardo, F. Meriaudeau, T. P. Karnowski, Y. Li, S. Garg, K. W. Tobin, and E. Chaum, "Exudate-based diabetic macular edema detection in fundus images using publicly available datasets," *Medical image analysis*, vol. 16, no. 1, pp. 216–226, 2012.
- [22] Z. Feng, J. Yang, L. Yao, Y. Qiao, Q. Yu, and X. Xu, "Deep retinal image segmentation: A fcn-based architecture with short and long skip connections for retinal image segmentation," in *International Conference on Neural Information Processing*. Springer, 2017, pp. 713–722.
- [23] R. Srivastava, J. Cheng, D. W. Wong, and J. Liu, "Using deep learning for robustness to parapapillary atrophy in optic disc segmentation," in *Biomedical Imaging (ISBI), 2015 IEEE 12th International Symposium on*. IEEE, 2015, pp. 768–771.

- [24] R. Caruana, "Multitask learning," *Machine learning*, vol. 28, no. 1, pp. 41–75, 1997.
- [25] X.-T. Yuan, X. Liu, and S. Yan, "Visual classification with multitask joint sparse representation," *IEEE Transactions on Image Processing*, vol. 21, no. 10, pp. 4349–4360, 2012.
- [26] T. Zhang, B. Ghanem, S. Liu, and N. Ahuja, "Robust visual tracking via structured multi-task sparse learning," *International journal of computer vision*, vol. 101, no. 2, pp. 367–383, 2013.
- [27] Y. Yan, E. Ricci, R. Subramanian, G. Liu, and N. Sebe, "Multitask linear discriminant analysis for view invariant action recognition," *IEEE Transactions on Image Processing*, vol. 23, no. 12, pp. 5599–5611, 2014.
- [28] Y. Yan, E. Ricci, G. Liu, and N. Sebe, "Egocentric daily activity recognition via multitask clustering," *IEEE Transactions on Image Processing*, vol. 24, no. 10, pp. 2984–2995, 2015.
- [29] X. Zhang, G. Thibault, E. Decencière, B. Marcotegui, B. Laÿ, R. Danno, G. Cazuguel, G. Quellec, M. Lamard, P. Massin et al., "Exudate detection in color retinal images for mass screening of diabetic retinopathy," *Medical image analysis*, vol. 18, no. 7, pp. 1026–1043, 2014.
- [30] T. Kauppi, V. Kalesnykiene, J.-K. Kamarainen, L. Lensu, I. Sorri, A. Ranninen, R. Voutilainen, H. Uusitalo, H. Kälviäinen, and J. Pietilä, "The diaretdb1 diabetic retinopathy database and evaluation protocol." in *BMVC*, 2007, pp. 1–10.
- [31] E. J. Carmona, M. Rincón, J. García-Feijoó, and J. M. Martínez-de-la Casa, "Identification of the optic nerve head with genetic algorithms," *Artificial Intelligence in Medicine*, vol. 43, no. 3, pp. 243–259, 2008.
- [32] E. Decencière, X. Zhang, G. Cazuguel, B. Laÿ, B. Cochener, C. Trone, P. Gain, R. Ordonez, P. Massin, A. Erginay et al., "Feedback on a publicly distributed image database: the messidor database," *Image Analysis & Stereology*, vol. 33, no. 3, pp. 231–234, 2014.
- [33] R. Kälviäinen and H. Uusitalo, "Diaretdb1 diabetic retinopathy database and evaluation protocol," in *Medical Image Understanding and Analysis*, vol. 2007. Citeseer, 2007, p. 61.
- [34] R. Zheng, L. Liu, S. Zhang, C. Zheng, F. Bunyak, R. Xu, B. Li, and M. Sun, "Detection of exudates in fundus photographs with imbalanced learning using conditional generative adversarial network," *Biomedical Optics Express*, vol. 9, no. 10, pp. 4863–4878, 2018.
- [35] P. Chudzick, S. Majumdar, F. Calivá, B. Al-Diri, and A. Hunter, "Microaneurysm detection using fully convolutional neural networks," *Computer methods and programs in biomedicine*, vol. 158, pp. 185–192, 2018.
- [36] O. Ronneberger, P. Fischer, and T. Brox, "U-net: Convolutional networks for biomedical image segmentation," in *International Conference on Medical Image Computing and Computer-Assisted Intervention*. Springer, 2015, pp. 234–241.
- [37] K.-K. Maninis, J. Pont-Tuset, P. Arbeláez, and L. Van Gool, "Deep retinal image understanding," in *International Conference on Medical Image Computing and Computer-Assisted Intervention*. Springer, 2016, pp. 140–148.
- [38] S. Xie and Z. Tu, "Holistically-nested edge detection," in *Proceedings of the IEEE international conference on computer vision*, 2015, pp. 1395–1403.
- [39] C. Wolf and J.-M. Jolion, "Object count/area graphs for the evaluation of object detection and segmentation algorithms," *International Journal of Document Analysis and Recognition (IJ DAR)*, vol. 8, no. 4, pp. 280–296, 2006.
- [40] S. Ruder, "An overview of multi-task learning in deep neural networks," *arXiv preprint arXiv:1706.05098*, 2017.
- [41] J. Baxter, "A bayesian/information theoretic model of learning to learn via multiple task sampling," *Machine learning*, vol. 28, no. 1, pp. 7–39, 1997.
- [42] T. Walter, J.-C. Klein, P. Massin, and A. Erginay, "A contribution of image processing to the diagnosis of diabetic retinopathy-detection of exudates in color fundus images of the human retina," *IEEE transactions on medical imaging*, vol. 21, no. 10, pp. 1236–1243, 2002.
- [43] M. Abdullah, M. M. Fraz, and S. A. Barman, "Localization and segmentation of optic disc in retinal images using circular hough transform and grow-cut algorithm," *PeerJ*, vol. 4, p. e2003, 2016.
- [44] S. Morales, V. Naranjo, J. Angulo, and M. Alcañiz, "Automatic detection of optic disc based on pca and mathematical morphology," *IEEE transactions on medical imaging*, vol. 32, no. 4, pp. 786–796, 2013.
- [45] M. N. Zahoor and M. M. Fraz, "Fast optic disc segmentation in retinal images using polar transform," in *Annual Conference on Medical Image Understanding and Analysis*. Springer, 2017, pp. 38–49.
- [46] M. M. Fraz, W. Jahangir, S. Zahid, M. M. Hamayun, and S. A. Barman, "Multiscale segmentation of exudates in retinal images using contextual cues and ensemble classification," *Biomedical Signal Processing and Control*, vol. 35, pp. 50–62, 2017.
- [47] B. Harangi and A. Hajdu, "Automatic exudate detection by fusing multiple active contours and regionwise classification," *Computers in biology and medicine*, vol. 54, pp. 156–171, 2014.
- [48] A. Kendall, Y. Gal, and R. Cipolla, "Multi-task learning using uncertainty to weigh losses for scene geometry and semantics," *arXiv preprint arXiv:1705.07115*, vol. 3, 2017.
- [49] X. Li, L. Zhao, L. Wei, M.-H. Yang, F. Wu, Y. Zhuang, H. Ling, and J. Wang, "Deepsaliency: Multi-task deep neural network model for salient object detection," *IEEE Transactions on Image Processing*, vol. 25, no. 8, pp. 3919–3930, 2016.
- [50] S. Li, Z.-Q. Liu, and A. B. Chan, "Heterogeneous multi-task learning for human pose estimation with deep convolutional neural network," in *Proceedings of the IEEE conference on computer vision and pattern recognition workshops*, 2014, pp. 482–489.

...